

Multimodal Laryngoscopic Video Analysis for Assisted Diagnosis of Vocal Fold Paralysis

Yucong Zhang, Xin Zou, Jinshan Yang, Wenjun Chen, Juan Liu, Faya Liang* and Ming Li*

Abstract—This paper presents the Multimodal Laryngoscopic Video Analyzing System (MLVAS)¹, a novel system that leverages both audio and video data to automatically extract key segments and metrics from raw laryngeal videostroboscopic videos for assisted clinical assessment. The system integrates video-based glottis detection with an audio keyword spotting method to analyze both video and audio data, identifying patient vocalizations and refining video highlights to ensure optimal inspection of vocal fold movements. Additionally, MLVAS features an advanced strobing video extraction module that specifically identifies strobing frames from laryngeal videostroboscopy by analyzing hue, saturation, and value fluctuations. Beyond key segment extraction, MLVAS provides effective metrics for Vocal Fold Paralysis (VFP) detection. It employs a novel two-stage glottis segmentation process using a U-Net for initial segmentation, followed by a diffusion-based refinement to reduce false positives, providing better segmentation masks for downstream tasks. MLVAS estimates the vibration dynamics for both left and right vocal folds from the segmented glottis masks to detect unilateral VFP by measuring the angle deviation with the estimated glottal midline. Comparing the variance between left's and right's dynamics, the system effectively distinguishes between left and right VFP. We conducted several ablation studies to demonstrate the effectiveness of each module in the proposed MLVAS. The experimental results on a public segmentation dataset show the effectiveness of our proposed segmentation module. In addition, VFP classification results on a real-world clinic dataset demonstrate MLVAS's ability of providing reliable and objective metrics as well as visualization for assisted clinical diagnosis.

Index Terms—Glottis Segmentation, Keyword Spotting, Laryngoscope, Vocal Fold Paralysis

(The first two authors contributed equally to this work.)(Corresponding authors: Faya Liang and Ming Li.)(This study was approved by the Institutional Review Board of Sun Yat-sen Memorial Hospital of Sun Yat-sen University under no. SYSEC-KY-KS-2022-040 and the Institutional Review Board of Duke Kunshan University under no. 2022ML067.)

Yucong Zhang and Ming Li are with the School of Computer Science, Wuhan University, Wuhan 430072, China and the Suzhou Municipal Key Laboratory of Multimodal Intelligent Systems, Data Science Research Center, Duke Kunshan University, Suzhou 215316, China (e-mail: yucong.zhang@whu.edu.cn, ming.li369@dukekunshan.edu.cn)

Juan Liu is with the School of Computer Science, Wuhan University, Wuhan 430072, China (e-mail: liujuan@whu.edu.cn)

Faya Liang, Xin Zou, Jinshan Yang and Wenjun Chen are with the Sun Yat-sen Memorial Hospital of Sun Yat-sen University, Guangzhou 510000, China (e-mail: liangfy3@mail.sysu.edu.cn, zoux25@mail2.sysu.edu.cn, Lucky9812@163.com, 273147323@qq.com)

¹Demo available at <https://drive.google.com/file/d/1L1ZH2K3xZiQGFW-1ce89uH9LfYM-RWJH/view?usp=sharing>

I. INTRODUCTION

Vocal fold Paralysis (VFP) is a condition where one of the vocal folds fails to move properly, leading to voice changes, difficulty swallowing, and potential breathing problems [1], [2]. VFP can result from nerve damage due to surgery, injury, infection, or tumors, significantly impacting a patient's quality of life [3]. Accurate diagnosis of VFP is crucial, as it informs the appropriate medical or surgical intervention, which can restore vocal function, improve airway protection, and enhance overall patient outcomes. Clinicians often use laryngeal videostroboscopy to check the vocal fold vibration in details. Laryngeal videostroboscopy is a specialized diagnostic tool used to evaluate the function of the vocal folds and the larynx. The stroboscopic component is key because it allows for visualization of vocal fold vibrations, which are often too rapid to be observed directly by doctors [4]. Stroboscopy uses a light source that flashes at a slightly different frequency than the vocal fold vibration. This creates a slow-motion effect, enabling the clinician to see the individual phases of vocal fold vibration in great details.

With the advent of the artificial intelligence, deep learning methods are developed to extract useful parameters [5] to assist clinicians track the motion of vocal folds [6]–[10], and even make predictions [11], [12] or classifications [13] to help clinicians perform diagnosis. However, the diagnosis of VFP requires to inspect the complete phonation cycles of patients. Previous works default to using video frames or images that already contain the vocal folds, but in most of the time, the raw recordings from the endoscopic inspection often carry useless information other than patient's phonation cycles. For instance, no phonation cycles occur in the beginning of the inspection, as the laryngoscope is still finding the vocal folds.

Although experienced experts can provide valuable insights through the analysis of endoscopic videos, this approach often relies on subjective diagnosis, which can compromise objectivity and increase patient anxiety, as well as heighten the risk of misdiagnosis. To address these challenges, various analytical methods have been developed to enhance the efficiency of diagnoses derived from endoscopic videos [14]–[17]. Notably, Gloger et al. focus on physical features such as color and shape to segment the glottic area [14], while Adamian et al. and Wang et al. employ supervised learning techniques to track vocal fold movements and derive the Anterior Glottic Angle (AGA), measuring the angle between the two vocal folds [15], [16]. By calculating the glottal area and AGA for

each frame, those aforementioned researchers show the Glottal Area Waveform (GAW) and the AGA waveform. However, these methods are limited as those two features essentially measure the gap between left and right vocal folds and therefore cannot indicate which specific vocal fold is paralyzed, rendering them ineffective for diagnosing Unilateral Vocal Fold Paralysis (UVFP). While Pennington et al. expand on feature extraction by including a greater variety of metrics, their methods still derive primarily from the AGA, which limits their applicability for UVFP detection [17]. Additionally, these methods are confined to pre-processed or short video segments without stroboscopic examinations, making the analysis of raw and lengthy laryngoscopic videos in real clinical settings particularly challenging. Consequently, preliminary annotation work is still required in the aforementioned methods, which adds to the inconvenience for clinical experts.

Existing approaches rely solely on video modalities, neglecting the potential benefits of incorporating audio data, which could enhance diagnostic precision. Audio-related methods have shown great potential to detect voice pathology as well [18]–[20]. Such methods typically involve converting audio clips to spectrograms using short-time Fourier transform (STFT), which are then fed into various models for downstream tasks. For instance, Deep Neural Networks (DNN) is utilized to predict vocal fold pathology [21]–[24]. Low et al. build a machine learning model to detect anomalous patterns in the spectrogram [25]. Compton et al. use an Artificial Neural Network (ANN) to predict vocal fold pathology, claiming to outperform expert assessments [26]. However, these approaches focus solely on the patient’s audio data, without the crucial visual information, which contains more explainable and comprehensive insights into vocal fold conditions.

In this article, we present the Multimodal Laryngoscopic Video Analyzing System (MLVAS), which is a novel system that leverages both the audio and video modalities to automatically process raw laryngeal videostroboscopic videos. The main contributions of our work are listed as follows.

1. **Multimodal Video Extraction:** We propose a system that integrates an audio-based Keyword Spotting (KWS) mechanism to automatically extract valid video segments containing complete phonation cycles and strobing segments from raw laryngeal videostroboscopic videos, effectively reducing the time clinicians spend reviewing lengthy video recordings.
2. **Two-Stage Segmentation Pipeline:** A robust two-stage glottis segmentation framework is developed, utilizing a U-Net model for initial segmentation followed by a diffusion-based refinement stage, which significantly reduces false alarms and enhances segmentation precision.
3. **Metrics for UVFP Detection:** The system introduces Left and Right Vocal Fold Dynamics (LVFDyn and RVFDyn) for UVFP detection. These metrics measure the angle derivation for both sides of the vocal folds through time, which show great potential in UVFP diagnosis.

The organization of this paper is as follows: Section II reviews some related works about U-Net based image segmentation and metric computation for UVFP. Section III details our

proposed method for key video segment extraction, including audio keyword spotting, visual glottis detection, and strobing segment detection. Section IV and Section V focus on the vocal fold analysis module on top of the selected key segments. More specifically, Section IV presents the two-stage glottis image segmentation technique, including the initial U-Net segmentation and the diffusion based second-pass refinement. Section V describes our method to detect VFP and UVFP, including metric computation, glottal midline estimation, and audio-visual VFP detection, respectively. Finally, section VI presents experimental results, and Section VII concludes the paper.

II. RELATED WORKS

A. U-Net Based Glottis Image Segmentation

U-Net’s encoder-decoder structure with skip connections has been proved as a robust framework for biomedical image segmentation [27], [28]. Modifications to this architecture, such as the introduction of separable convolutions in S3AR U-Net [29] and the incorporation of attention mechanisms in Attention U-Net [30], have demonstrated improved performance by capturing more salient features and reducing computational demands. The pursuit of efficiency and clinical applicability has led to the development of models like Efficient U-Net [31], which offers a low inference complexity while maintaining high segmentation quality. Yet, the trade-off between segmentation accuracy and computational cost is a recurring theme, with models like VGG19 U-Net [31] showing longer inference times. Despite the computational efficiency of U-Net variants, the need for substantial labeled training data and the potential for overfitting remain concerns [32]. To counter this, weakly supervised learning approaches, like the one proposed by [33], have gained attraction, requiring only point annotations and demonstrating a remarkable balance between segmentation accuracy and convergence speed.

While the field has made significant strides, challenges persist in achieving a harmonious balance between segmentation accuracy, and generalizability across varied clinical datasets. The limited size of the glottis segmentation mask often leads to a high incidence of false positives when using U-Net structures [34]–[36], resulting in segmentation outputs even in the absence of glottal regions. This can significantly impair the accuracy of subsequent analyses. To address this issue, we incorporate a diffusion model as the second-pass refinement, which further enhances the precision of the initial U-Net based segmentation results.

B. UVFP Detection and glottal midline Estimation

In initial investigations, researchers found that the maximum separation between vocal folds and UVFP are significantly correlated [37]. As studies progressed, the GAW and AGA emerged as key metrics for quantifying this separation, thereby playing a pivotal role in VFP detection. However, existing methodologies typically evaluate those two metrics without distinguishing between the left and right vocal folds [12], [15], [16], [38]. To overcome this limitation, we introduce Vocal Fold Dynamics (VFDyn), including LVFDyn and RVFDyn,

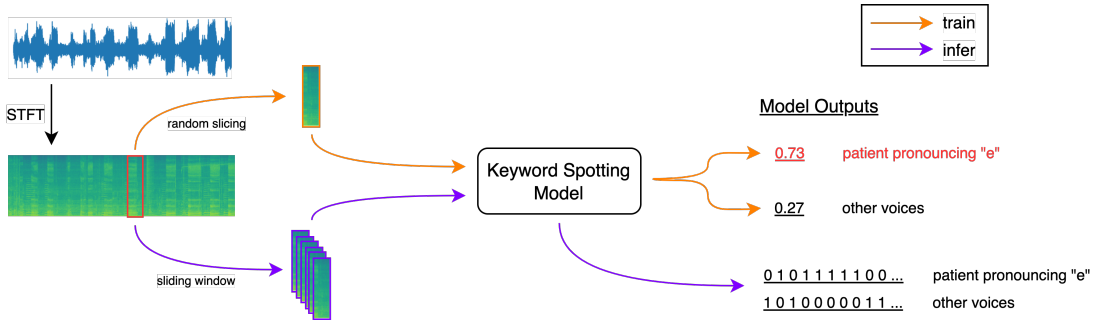


Fig. 1: The overview of the audio processing module. The orange line shows the training process, and the purple line shows the inferring process.

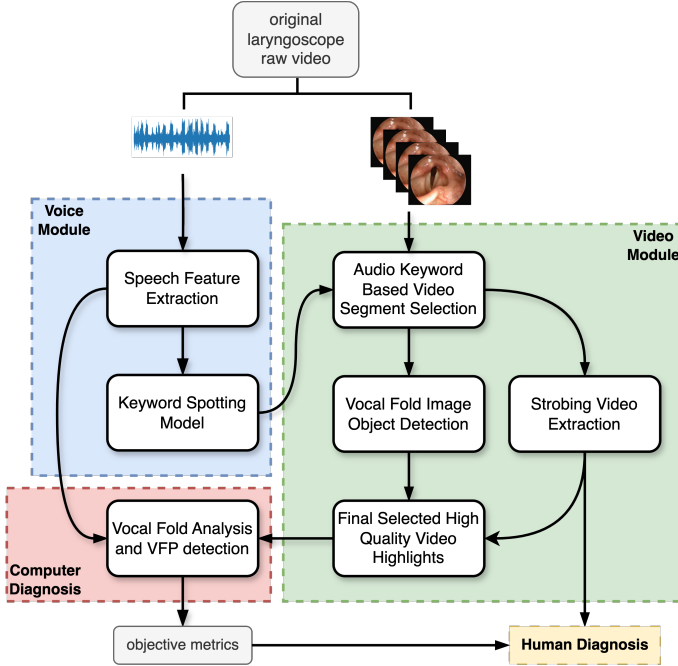


Fig. 2: The overview of our proposed MLVAS framework.

assessing the left and right vocal fold angle deviations to the estimated glottal midline. By comparing VFDyn of two vocal folds, our experimental results on actual clinical data indicate that it is possible to effectively differentiate between left and right vocal fold paralysis.

However, assessing the motion of the left and right vocal folds requires accurately identifying the glottal midline, as LVFDyn and RVFDyn represent angle deviations from the midline through time. Traditional methods often depend on extensive labelled datasets for supervised learning [39], [40], which can be labor-intensive. In contrast, our approach autonomously estimates the midline of the glottal area without necessitating any annotated data.

III. MULTIMODAL KEY SEGMENT EXTRACTION

A. System Design

Our system aims to facilitate efficient clinical examinations by extracting key segments from laryngoscopic videos and providing objective indicators for specific laryngeal diseases. As Fig. 2 shows, comprising two main modules – the voice module, the video module – our system ensures the accurate

observation of vocalization cycles and the clear visualization of the glottal area.

The voice module initially processes the audio extracted from the video using Short-Time Fourier Transform (STFT) to obtain spectrograms. Through KWS technique, each frame is analyzed to detect patient vocalizations. This enables the preliminary segmentation of vocalization segments within the video.

Subsequently, the video module further refines these vocalization segments to obtain key segment to form laryngoscopic highlights, ensuring the visibility of the vocal folds. Specifically, by utilizing the glottis object detection model, MLVAS can identify regions containing the vocal folds and glottis in each frame. Moreover, given the importance of the stroboscopic portions in laryngoscopic videos for subjective analysis by physicians, we also include a stroboscopic video extraction method into our system.

B. Audio Processing Module

To get a better examination of the status of the vocal folds, patients are often pronouncing “e” (although asked to pronounce “a”) while the clinicians examine the larynx using the endoscope. In this way, the vibration of the vocal folds can be easily been detected by the clinicians. Hence, by capturing the audio segments that pronounce “e”, phonation cycles can be detected. To accomplish this, we developed a KWS model that is used to detect audio keywords in a sentence, such as “Hey Siri”, “Ok Google”, and in our case, the word “e”.

The overall pipeline is illustrated in Fig. 1. Initially, the input audio is transformed into a STFT spectrogram, converting the time-domain signal into a time-frequency representation for more effective analysis. The spectrogram is then segmented into chunks along the time axis, with each chunk containing a fixed number of frames. During the training phase, these chunks are randomly selected from each audio clip to ensure a diverse set of training samples. This method enhances the model’s generalization capabilities by incorporating spectrograms from various audio clips into a robust batch of training data.

The spectrogram chunks are subsequently fed into the KWS model, the architecture of which is detailed in TABLE I. The model comprises multiple convolutional blocks and residual blocks [41], designed to efficiently extract relevant features from the spectrogram chunks. Within the model, we use

TABLE I: Model structure for keyword spotting

Operator	# of out channels	Kernel	stride
Conv2D	32	(3,3)	(1,1)
MaxPool2D	-	(1,1)	(1,1)
ResNet2D	64	(3,3)	(1,1)
MaxPool2D	-	(2,2)	(2,2)
ResNet2D	64	(3,3)	(1,1)
MaxPool2D	-	(1,1)	(1,1)
ResNet2D	128	(3,3)	(1,1)
MaxPool2D	-	(2,2)	(2,2)
ResNet2D	128	(3,3)	(1,1)
MaxPool2D	-	(1,1)	(1,1)
AdaptiveAvgPool2D	-	-	-
Linear	32	-	-
Linear	2	-	-

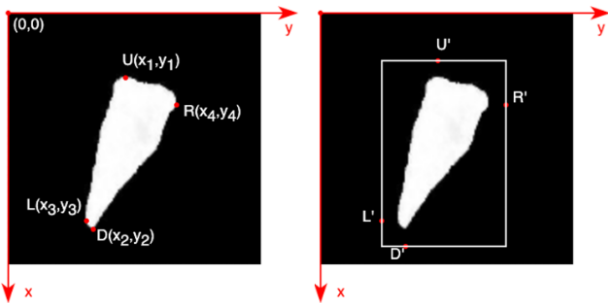


Fig. 3: The workflow of bounding box label generation. U' , R' , L' , D' are the extended points of U , R , L , D respectively.

max pooling to progressively reduce the spatial dimensions. Furthermore, we use an adaptive average pooling layer to aggregate the features before they pass through two fully connected layers, with the final layer producing the classification score output.

During the inference, the input spectrogram is sliced into chunks using a sliding window mechanism. Each chunk is processed by the trained KWS model to generate decision results, as depicted in Fig. 1. This KWS model can reliably detect the "ee" vocalization, providing critical prior knowledge for the subsequent analysis.

C. Video Processing Module

Although the audio KWS model is employed to detect the vocalization video segment of the phonation "e", these detected video segments may not always successfully capture the vocal folds and glottis on the visual side. To address this issue, we train a vocal fold detection model, utilizing the famous object detection model structure YOLO-v5 [42], to further refine the time masks.

Given the limitations of the open-source data for training a detection model, we utilize the public glottis segmentation dataset, BAGLS [43], to construct our training dataset. Since BAGLS is a glottis segmentation dataset, it only contains mask labels for the glottis. To generate labels for vocal fold detection, we designed an automatic bounding box generator. As illustrated in Fig. 3, the process begins by obtaining the coordinates of the top, bottom, left, and right vertices from the glottis mask. These coordinates are denoted as $U(x_1, y_1)$,

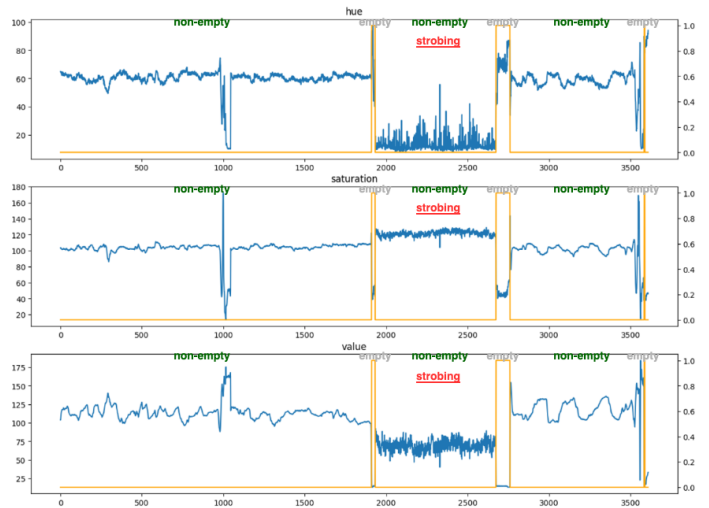


Fig. 4: An example result of the HSV analysis for strobing video extraction. The blue line represents the HSV values along the time axis. The yellow line is the unit step function highlighting the empty frames with zero values.

$D(x_2, y_2)$, $L(x_3, y_3)$, and $R(x_4, y_4)$, respectively. Next, these vertices are manually expanded by a fixed number of pixels to ensure adequate coverage around the vocal folds, denoted as U' , D' , L' , and R' . Using the expanded points, a bounding box is computed, as shown on the right side of Fig. 3.

As depicted in Fig. 2, our pipeline integrates a strobing video extraction module alongside the vocal fold image object detection module. This module is utilized to select the strobing segments of laryngeal videos by analyzing hue, saturation, and value (HSV) of video frames. The HSV parameters represent type, intensity, and brightness of colors, respectively. Transitions marked by empty frames typically occur at the beginning and end of strobing segments. We employ a unit step function to identify and mark all empty frames with a zero value in color (illustrated by the yellow line in Fig. 4). This technique segments the video into several continuous non-empty frame sequences. Within these non-empty segments, we examine the variations in HSV values. The variations is calculated as the total number of changes within a time range. Due to the rapid color-changing characteristic of strobing videos (as shown in Fig. 4), we are able to identify the strobing segments by calculating the frequency of HSV fluctuations within each non-empty segment, selecting the segment with the highest number of fluctuations. Suppose v_{t-1}, v_t, v_{t+1} stands for the value at time step $t-1, t$ and $t+1$ respectively. Then, the frequency of HSV fluctuation within a time range of $T = [t_0, t_n]$ is calculated as follows.

$$F_T = \sum_{t=1}^{n-1} \frac{(v_t - v_{t-1}) * (v_{t+1} - v_t)}{|(v_t - v_{t-1}) * (v_{t+1} - v_t)|}$$

IV. GLOTTIS IMAGE SEGMENTATION

In the evaluation of laryngeal function and pathology, accurate image segmentation of the glottis is essential. This segmentation enables the extraction of objective metrics that clinicians can utilize for diagnosis and review. In our system, we implement a two-stage approach comprising a U-Net-based

TABLE II: Model structure for the U-Net model

Operator	CH	Kernel	Stride
ConvBlock	64	(3,3)	(1,1)
MaxPool2D	-	(2,2)	-
ConvBlock	128	(3,3)	(1,1)
MaxPool2D	-	(2,2)	-
ConvBlock	256	(3,3)	(1,1)
MaxPool2D	-	(2,2)	-
ConvBlock	512	(3,3)	(1,1)
UpSample	-	-	-
ConvBlock	256	(3,3)	(1,1)
UpSample	-	-	-
ConvBlock	128	(3,3)	(1,1)
UpSample	-	-	-
ConvBlock	64	(3,3)	(1,1)
ConvBlock	1	(1,1)	(1,1)

TABLE III: Model structure for the ConvBlock

Operator	# of out channels	Kernel
Conv2D	CH	(3,3)
BatchNorm2D	CH	-
Conv2D	CH	(3,3)
BatchNorm2D	CH	-
ReLU	-	-

method followed by a diffusion-based refinement. The initial segmentation is performed using a naive U-Net model, which is simple yet effective in medical image segmentation tasks. This model provides a robust initial estimate of the glottis boundaries.

However, the U-Net model tends to produce false positives, especially in cases where the glottal area is not visible (see Table V). These incorrect segmentation can complicate subsequent vocal fold analysis modules. To address this issue and enhance the precision of the segmentation results, we further refine the U-Net outputs using a diffusion model. This additional step helps to correct the errors and produce a more accurate and reliable glottis mask. The combination of these two methods ensures high-quality segmentation, which is crucial for subsequent analysis and metric computation.

The following subsections provide detailed descriptions of each component in our glottis segmentation pipeline, including the U-Net-based method and the diffusion-based refinement.

A. U-Net-based Method

The U-Net model is a convolutional neural network specifically designed for biomedical image segmentation. Owing to its effectiveness and accuracy, we employ a U-Net as our segmentation model. As shown in Table II, the model comprises a series of convolutional blocks, referred to as ConvBlocks (see Table III), which include convolution operations followed by batch normalization and ReLU activation functions. The U-Net architecture is symmetrical, featuring a contracting path that captures contextual information and an expansive path that facilitates precise localization through upsampling operations. The contracting path consists of ConvBlocks with progressively increasing numbers of channels (64, 128, 256, and 512), interspersed with MaxPool2D layers for downsampling.

This is followed by a sequence of upsampling operations and ConvBlocks that reduce the feature map dimensions, effectively reconstructing the image to its original resolution. The final layer utilizes a ConvBlock with a single output channel to generate the segmentation mask.

There are several advantages to using a U-Net model with this structure. First, the architecture captures both low-level and high-level features through its deep structure and skip connections, which concatenate features from the contracting path to the corresponding layers in the expansive path. This facilitates precise segmentation by preserving spatial information. Second, the use of ConvBlocks with batch normalization stabilizes and accelerates the training process, while ReLU activation functions introduce non-linearity, enabling the model to learn complex patterns. Additionally, the upsampling layers allow for finer segmentation outputs by gradually reconstructing the image details.

B. Diffusion Model-based Refinement

The U-Net model excels at extracting image masks. However, the generated masks may tend to yield false alarms (see Table V). To further enhance the quality, we explore the integration of the diffusion model. Diffusion models are generative models, which proves to be very powerful tools for generating high-quality images [44], [45]. These models are designed to generate images by iteratively denoising random noise to match a target distribution, allowing them to produce diverse outputs while still maintaining a coherent structure or theme. By incorporating the diffusion model as a post refinement step, we expect the glottis mask extracted by U-Net to be further optimized with the diversity introduced.

Diffusion models consist of two stages: forward diffusion and reverse diffusion. During the forward process, Gaussian noise is gradually added to the segmentation label x_0 over a series of steps T . Conversely, in the reverse process, a neural network is trained to recover the original data by reversing the noise addition, as represented by the following equation:

$$p_{\theta}(x_{0:T-1} | x_T) = \prod_{t=1}^T p_{\theta}(x_{t-1} | x_t), \quad (1)$$

where θ stands for the parameters for the reverse process.

Consistent with the conventional implementation of the Diffusion Probability Model (DPM) [44], a U-Net model is employed for training. As Fig. 5 is shown, following the idea of MedSegDiff [46], we incorporate the original glottis images as priors for the step estimation function and employ dynamic conditional encoding to fuse the encoding outcomes from both the raw image and the segmentation mask at each step. Hence, for each step, the estimation function ϵ_{θ} is written as:

$$\epsilon_{\theta}(x_t, I, t) = D((E_t^I + E_t^x, t), t), \quad (2)$$

where θ stands for the learning parameters, D is the decoder, I is the raw image prior, t is the current diffusion step. E_t^I and E_t^x are the embeddings encoded from the raw image and segmentation mask at step t respectively.

Different from the traditional training procedure, we do not start the diffusion process from a standard Gaussian noise,

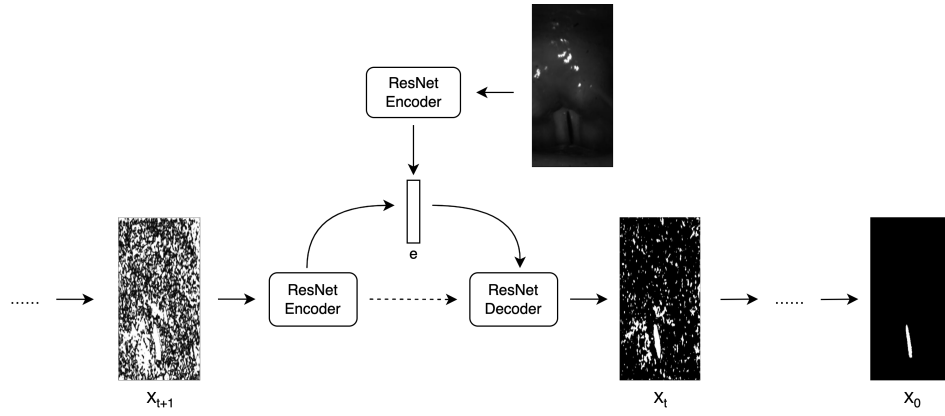


Fig. 5: The overview of the second-pass diffusion-based refinement. The denoising process starts from a customized Gaussian noise, utilizing the glottis mask generated by the first-pass U-Net glottis segmentation.

Algorithm 1 Angle Deviation Extraction Algorithm

Require: Glottis mask vertices' coordinates $U(x_1, y_1)$, $D(x_2, y_2)$, $L(x_3, y_3)$, $R(x_4, y_4)$

Ensure: Glottal angles $\{\angle L_k D' C\}_{k \in [1, N-1]}$, $\{\angle C D' R_k\}_{k \in [1, N-1]}$

- 1: Compute the center $C(x_c, y_c)$ from U, D, L, R
- 2: Compute the function $f(x)$ passing through C, D
- 3: Find N equidistant points C_1, C_2, \dots, C_{N-1} of $f(x)$ on the line segment intercepted by the glottal mask
- 4: **for** $k = 1$ to $N - 1$ **do**
- 5: Compute the function $f'_k(x)$ orthogonal to $f(x)$ passing through C_k
- 6: Compute intersection points L_k, R_k between $f'_k(x)$ and the glottis mask
- 7: **end for**
- 8: Rotate the coordinate system by γ degree to make $f(x)$ vertically aligned
- 9: Approximate a quadratic curve $q_\gamma(x)$ using rotated intersection points $\{L_{\gamma,k}\}_{k \in [1, N-1]}$ and $\{R_{\gamma,k}\}_{k \in [1, N-1]}$ in the rotated coordinate system
- 10: Find the vertex point D_q of $q_\gamma(x)$ and map D_q to the original coordinate system
- 11: Connect C and D_q to form the corrected middle line $f^*(x)$ and intersect the glottis mask at D'
- 12: Connect $\{L_k\}_{k \in [1, N-1]}$ and $\{R_k\}_{k \in [1, N-1]}$ with D' to obtain glottal angles

$p_\theta(x_T) = \mathcal{N}(x_T; \mathbf{0}, I_{n \times n})$ for an $n \times n$ image. Instead, by integrating the U-Net result introduced in Section IV-A, we start the diffusion process from a customized Gaussian noise, which is:

$$p_\theta(x_T) = \mathcal{N}(x_T; \mu', I_{n \times n}), \quad (3)$$

$$\mu' = (1 - (\alpha \cdot (1 - m') + (1 - \alpha) \cdot m')) \times 10^{-3}, \quad (4)$$

where $\alpha \sim U(0, 0.3)$ is a random parameter sampled from a uniform distribution, m' is the mask generated by the U-Net model in Section IV-A.

We determine the new mean for the Gaussian noise in the diffusion process by computing the weighted average between the glottis mask initially generated by U-Net and its comple-

ment (see Equation 4). This essentially guides the diffusion process to pay more attention to areas outside the glottal region, encouraging the model to refine the segmentation boundaries for improved accuracy.

V. MULTIMODAL VOCAL FOLD PARALYSIS ANALYSIS

To detect VFP, we adopt a two-stage process. First, we build a binary classification model to check if it belongs to VFP. Then, with our proposed metrics, left and right VFP can be identified by comparing the left and right vocal fold movement via the plots.

A. Vocal Fold Dynamic Extraction with Quadratic Fitting

To diagnose the laryngeal paralysis in a more detailed way, instead of AGA or GAW that measures the both left and right vocal folds, we evaluate the angle deviation for each vocal fold. As a result, we can provide the contrastive diagnosis of unilateral laryngeal paralysis. The procedure for extracting glottal angles from a segmented glottis involves a systematic series of steps, detailed in Algorithm 1, with visual representations of the intermediate results provided in Fig. 6.

Initially, the algorithm acquires the coordinates of the top, bottom, left, and right vertices from the glottis mask, computing their center point denoted as $U(x_1, y_1)$, $D(x_2, y_2)$, $L(x_3, y_3)$, $R(x_4, y_4)$, and $C(x_c, y_c)$ respectively (see Fig. 6(a)). Subsequently, a line connecting points C and D is established, and a linear function $f(x)$ passing through C and D is computed.

Equidistant points C_1, C_2, \dots, C_{N-1} are then positioned along the line segment intercepted by the glottal mask. For each C_k , orthogonal functions $f'_k(x)$ to $f(x)$ are calculated, with their intersection points L_k and R_k with the glottis mask determined for $k \in [1, N - 1]$ (see Fig. 6(b)).

To ensure uniformity, the coordinate system is rotated by an angle γ , aligning all intersection points along the y-axis after rotation, denoted as $L_{\gamma,k}$ and $R_{\gamma,k}$. Leveraging these points, a quadratic curve $q_\gamma(x)$ is approximated in the rotated coordinate system (see Fig. 6(c)). The lowest point D_q of $q_\gamma(x)$ is identified and mapped back to the original coordinate system (see Fig. 6(d)).

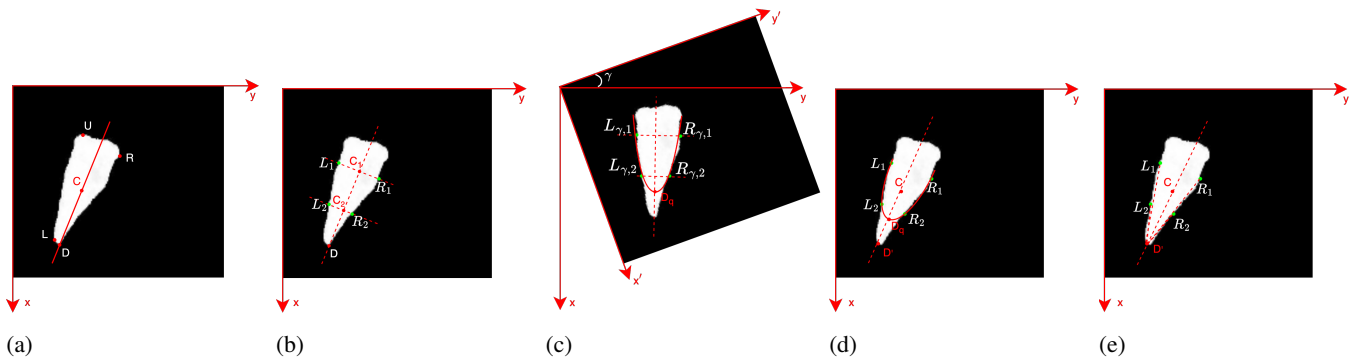


Fig. 6: The workflow of computing the angle deviation of left and right vocal folds. Step (a) get the center point C and bottom point D . Step (b), (c) and (d) fit the outline of vocal folds with a quadratic function, refining the bottom point to D' . As a result, step (e) shows the refined midline CD' . Finally, the angle deviation for both vocal folds can be computed.

Subsequently, a calibrated middle line $f^*(x)$ connecting points C and D_q is established, intersecting the glottis mask at point D' . Finally, glottal angles are derived by connecting points $\{L_k\}_{k \in [1, N-1]}$ and $\{R_k\}_{k \in [1, N-1]}$ with D' , yielding $\{\angle L_k D' C\}_{k \in [1, N-1]}$ and $\{\angle C D' R_k\}_{k \in [1, N-1]}$ respectively.

across all channels, while the LSTM layer processes temporal information effectively.

To further differentiate between left or right VFP, we analyze the variance of the LVFDyn and the RVFDyn time series. Intuitively, the paralyzed side exhibits less activity during phonation, leading to a smoother time sequence and consequently a lower variance. Therefore, by simply comparing the variance of left and right, we should be able to distinguish between left or right VFP.

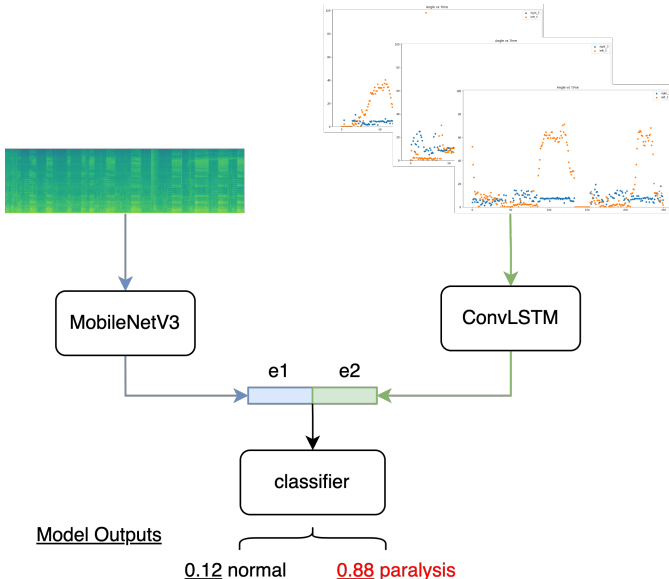


Fig. 7: The pipeline of the multimodal VFP classification model.

B. Multimodal Vocal Fold Paralysis Detection

We developed a model that integrates both audio and video modalities for the enhanced VFP detection. As illustrated in Fig. 7, the model utilizes the audio spectrograms and the Vocal Fold Dynamics (VFDyn) as inputs. The audio spectrogram is encoded using EfficientNet-b0 [47], a compact and efficient model renowned for its performance in image classification tasks. Given that multiple video highlights are extracted from a single laryngoscope video, with corresponding VFDyn for each, multiple time series are generated. These time series are treated as multi-channel inputs to a ConvLSTM [48] model, comprising a convolutional layer followed by an LSTM layer. The ConvLSTM model is adept at handling multi-channel time series; the convolutional layer captures features

VI. EXPERIMENTAL RESULTS

A. BAGLS Dataset

We use the Benchmark for Automatic Glottis Segmentation (BAGLS) [43] as the dataset for evaluating glottis image segmentation. It consists of 59,250 endoscopic glottis images acquired from hundreds of individuals at seven hospitals, which is split into 55,750 training images and 3,500 test images. In this paper, we follow the same data split as [43] to train the U-Net model and the diffusion model. Since the dataset only contains segmentation mask labels instead of bounding boxes covering the vocal folds, we utilize those labels to generate bounding boxes for vocal fold object detection.

B. SYSU Dataset

This dataset was collected in real-world clinical settings by the Sun Yat-sen Memorial Hospital of Sun Yat-sen University (SYSU). This study was approved by the Institutional Review Board of Sun Yat-sen Memorial Hospital of Sun Yat-sen University under no. SYSEC-KY-KS-2022-040 and the Institutional Review Board of Duke Kunshan University under no. 2022ML067. The dataset is deliberately divided into two parts, SYSU-A and SYSU-B.

The SYSU-A dataset consists of 520 clinical video samples, including 106 normal cases and 414 paralysis cases (257 left VFP and 157 right VFP), and is used to evaluate the performance of the proposed MLVAS in UVFP detection. To ensure fairness, we deliberately select equal number of samples for each category for testing. Specifically, we randomly choose 75 samples, including 25 normal, 25 left VFP and 25 right VFP, for testing, and leave other samples for training. The

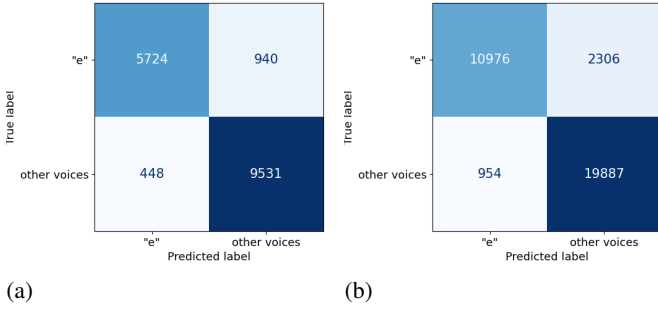


Fig. 8: The confusion matrices of the classification result of the audio KWS model using the best threshold with the highest F-score.

TABLE IV: The classification performance (%) of the KWS model on the full dataset of SYSU-A and the testing set of SYSU-B with the best threshold.

Dataset	# of samples	Accuracy(%)	Precision(%)	Recall(%)	F-score(%)
SYSU-A	34123	90.45	90.54	90.45	90.34
SYSU-B	16643	91.66	91.71	91.66	91.60

multi-modal VFP detection model is trained and tested on the SYSU-A dataset.

The SYSU-B dataset contains clinical video samples from cases other than VFP, e.g. vocal fold polyps and vocal fold nodules. We randomly split the SYSU-B dataset into training and testing subsets, assigning 80% of the samples for training and 20% for testing. The audio KWS model is trained and tested on the SYSU-B dataset, and its performance is then evaluated on the SYSU-A dataset. It should be noted that there is no overlap between the SYSU-A and SYSU-B datasets, ensuring the model can be applied to the full SYSU-A dataset for evaluation.

All videos were recorded using laryngeal videostroboscopes, with each clip containing at least one strobing video segment. The dataset reflects real-world variability, as the recordings were captured using different types of endoscopes across various locations, leading to domain shifts and posing challenges for algorithms to address.

C. Keyword Spotting Model

The detailed architecture of the KWS model is outlined in Table I. The audio input is represented by a Mel-spectrogram with 80 Mel filters, utilizing 1024 FFT points and a hop length of 512. A sliding window of 400 samples with a hop length of 64 samples is employed to extract frame-level features. During training, audio clips are randomly sampled from the SYSU-A dataset. For each selected audio clip, random chunks of 40 frames are extracted to form batches of training data. The model is trained over 100 epochs using the Adam optimizer with a learning rate of 0.005. During inference, a sliding window of 40 frames with a unit step size is used to process each audio clip in the test dataset.

Since the KWS model outputs a posterior score rather than a direct decision value, a threshold is necessary to determine

TABLE V: Glottis Image Segmentation Performance on the Testing Set of the BAGLS dataset.

	IoU	FAR
U-Net Baseline	0.77	15.8%
Diffusion-based	0.78	4.5%
U-Net w. diffusion refinement	0.80	2.0%

the final result. Consequently, the threshold is selected based on the highest F-score, a balanced metric that considers both precision and recall, providing a comprehensive measure of classification performance. In MLVAS, we pick a threshold of 0.38 as the classification boundary. If the posterior score output by the KWS model is higher than this value, the input chunk is regarded as "e". Otherwise, it is treated as other voices. Fig. 8a and Fig. 8b display the confusion matrix computed on the SYSU-A and SYSU-B dataset respectively. The accuracy, precision, recall and F-score are listed in Table. IV. As is shown in Table. IV, the performance of our audio KWS model are all above 90% on both the SYSU-A and SYSU-B.

D. Glottis Segmentation

We train the U-Net baseline with the same strategy as [43]. For the diffusion model, it is built on top of the model in [46], except that we slightly modify the noise to meet the prior knowledge of U-Net results. The diffusion step is set to 1,000. We train the diffusion model with 100,000 steps. The model is optimized by a AdamW optimizer with a learning rate of 0.0001.

We evaluate our segmentation model on the public glottis dataset BAGLS. We use Intersection over Union (IoU) as the metric, and the results are shown in Table. V. From the table, we can see that the diffusion model can have a slightly better IoU performance than the traditional U-Net, By refining the U-Net results with the diffusion ones, the IoU performance can be further improved.

Besides IoU, we also compute the False Alarm Rate (FAR) when using different segmentation methods. The False Alarm (FA) is defined as the situation where the glottis mask is detected when actually there is no glottis in the image. The FAR is calculated as the number of FA divided by the total number of images with no glottis. We care about FA as we need the segmentation masks for later analysis. FAs might produce wrong measurements and mislead the prediction results of VFP. From Table V, the traditional U-Net model shows a tendency to produce FA masks with a leading FAR of 15.8%. By contrast, diffusion-based segmentation model has a much lower FAR of 4.5%, which is more than two times lower. The result may indicates that, in terms of the glottis segmentation, the diffusion model performs more robust when dealing with image with no targets. Hence, after we refine the U-Net result with the diffusion model, we can further achieve a result with a lower FAR but a better IoU.

E. Vocal Fold Paralysis Detection

We performed ablation studies using various system configurations to evaluate the effectiveness of our proposed methods,

TABLE VI: Different system settings. The proposed system contains all the modules and uses all the modalities. System 1 is the naive system, using the images segmented by the U-Net baseline without quadratic fitting or diffusion refinement. System 2 adds the quadratic fitting module to the naive system. System 3 and System 4 are two systems with both proposed modules but using only one modality.

System	Quadratic Fitting	Diffusion-refinement	AGA Modality	Audio Modality
Proposed System	✓	✓	✓	✓
System 1	-	-	✓	✓
System 2	✓	-	✓	✓
System 3	✓	✓	-	✓
System 4	✓	✓	✓	-

TABLE VII: The average performance and its standard deviation (reported within the parenthesis) across the experiments using 4 different random seeds. All the experiments are conducted on the SYSU-A dataset.

Systems	Accuracy (%)	Precision (%)	Recall (%)	F-score (%)	Sensitivity (%)	Specificity (%)
System 1	73.00 (±2.45)	72.33 (±4.63)	76.00 (±8.00)	73.83 (±2.48)	76.00 (±8.00)	70.00 (±10.04)
System 2	77.67 (±1.51)	78.00 (±2.76)	77.33 (±4.13)	77.67 (±1.63)	77.33 (±4.13)	78.00 (±4.20)
System 3	73.67 (±2.34)	73.00 (±3.69)	75.33 (±1.63)	74.33 (±1.51)	75.33 (±1.63)	72.00 (±5.66)
System 4	66.33 (±4.63)	65.33 (±3.56)	69.33 (±12.56)	67.00 (±6.90)	69.33 (±12.56)	63.33 (±6.41)
Proposed System	81.33 (±3.27)	81.00 (±2.28)	82.00 (±7.04)	81.50 (±3.73)	82.00 (±7.04)	80.67 (±3.01)

TABLE VIII: We present the results of one-tailed t-tests between various system pairs, along with the corresponding t-values, degrees of freedom (df), and p-values, all at the 95% confidence level. These experiments are performed using the SYSU-A dataset, maintaining a consistent train-test split throughout.

Metric	Groups	Alternative hypothesis $\mu_0 < \mu$	t-value	df	p-value
Accuracy	Across modules	System 1 vs. System 2	3.96	8	0.0020
		System 1 vs. Proposed System	5.00	9	0.0003
		System 2 vs. Proposed System	2.50	7	0.0210
Across modalities	System 3 vs. Proposed System	System 3 vs. Proposed System	6.48	9	0.0001
		System 4 vs. Proposed System	4.68	9	0.0005
F-score	Across modules	System 1 vs. System 2	3.15	9	0.0058
		System 1 vs. Proposed System	4.19	9	0.0012
	Across modalities	System 2 vs. Proposed System	2.31	7	0.0272
		System 3 vs. Proposed System	4.53	8	0.0009
		System 4 vs. Proposed System	4.37	7	0.0016

as shown in Table VI. The experiments primarily focus on two aspects: first, the effectiveness of the modules for improving metric extraction, such as quadratic fitting and diffusion refinement, and second, the impact of multimodality on VFP detection performance. To validate the statistical significance of the performance improvements observed between different system configurations, a series of t-tests is conducted across different experimental trials with different random seeds. These pairwise t-tests are performed among various system configurations (shown in Table VIII), providing a p-value as a measure of statistical significance for the observed differences in performance metrics.

Modules vs. VFP Detection Performance

Accurate midline prediction is critical for analyzing left and right vocal fold movements, as it serves as a reference for measuring angle deviations and calculating distances between sample points on the vocal folds and the midline. However, in real-world applications, the laryngeal camera’s position is not

always fixed, complicating metric computation. Calibrating the midline by fitting a quadratic function has proven effective for improving midline prediction, leading to better classification performance. The associated results are detailed in Table VII. The system’s native setting serves as a foundational benchmark from which incremental enhancements are realized. The introduction of the proposed quadratic fitting method improves the accuracy from 73% to 78% and also enhances the specificity from 70% to 78%, significantly reducing the risk of misdiagnosing healthy patients. Further improvements are achieved by incorporating diffusion refinement into the glottis segmentation process. As indicated in Table VII, sensitivity grows from 77% to 82% and specificity further increases to 81%. The diffusion refinement is applied only to images where the glottis is not detected by the YOLO-v5 detector (discussed in Section III-C), as this technique specifically targets false alarms (FAs) in glottis detection (described in Section VI-D). By reducing false alarms, the overall performance of downstream VFP detection improves.

The paired t-test comparing System 1 and System 2 yields a p-value of 0.0020 for accuracy and 0.0058 for the F-score, indicating that quadratic fitting contributes to statistically significant improvement at the 5% significance level. The data also suggest that System 2, when compared to the proposed system, exhibits a p-value of 0.0210 for accuracy and 0.0272 for the F1-score, which underscores the positive effect of the diffusion-model based refinement. Additionally, the evaluation of our proposed system against System 1, characterized by basic settings, reveals profound enhancements in both accuracy and F-score, with p-values of 0.0003 and 0.0005 respectively, thereby affirming the combined efficacy of the proposed modules for VFP detection. To corroborate these findings, our analysis includes additional metrics such as t-values and degrees of freedom (df), further substantiating the significance of our advancements.

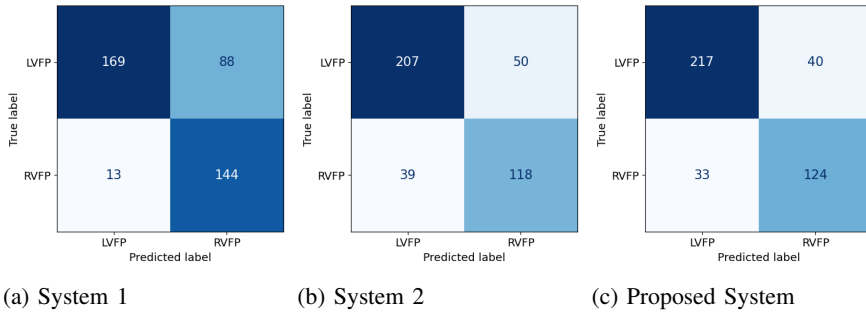


Fig. 9: Confusion matrix for the left or right VFP classification on the VFP cases of the SYSU-A dataset.

TABLE IX: Unilateral vocal fold paralysis classification through AGA comparison between left and right vocal folder

Systems	Accuracy (%)	Precision (%)	Recall (%)	F-score (%)
System 1	75.60	81.18	75.60	75.87
System 2	78.50	78.87	78.50	78.63
Proposed System	82.37	82.56	82.37	82.44

Multimodality vs. VFP Detection Performance

We also investigated the effect of multimodal inputs on VFP detection. When the AGA movement metrics were removed, classification performance decreased, with the F-score dropping to 74%, and sensitivity and specificity falling by an absolute value of 8.13% and 10.7%, respectively. These results highlight the importance of integrating both audio and AGA movement modalities for robust performance. Additionally, Table VII demonstrates the significant contribution of the audio modality in VFP detection, as excluding audio leads to a substantial drop in all evaluation metrics, with decreases of over 10%.

The t-tests conducted between the proposed multimodal system and the single-modality system are detailed in Table VIII. When comparing System 3 and System 4 to the proposed system, all performance metrics result in p-values lower than 0.05 and large t-values. This outcome indicates that the enhancements provided by the multimodal system are statistically significant at the 5% significance level and substantiates the efficacy of multimodal integration in VFP detection.

F. Detection of Unilateral Vocal Fold Paralysis

Through the analysis of variance in LVFDyn and RVFDyn, our approach can differentiate between left and right VFP within laryngeal stroboscopic videos. The performance of our detection system for UVFP is initially demonstrated on the SYSU-A dataset, where it effectively distinguishes between left and right VFP instances. Subsequently, the system's broader performance is evaluated across the entire dataset with the VFP detection results from the first-stage multimodal VFP analysis, providing a comprehensive view of MLVAS's real-world clinical applicability.

The classification results on the VFP cases from the SYSU-A dataset are summarized in Table IX, with the corresponding confusion matrix depicted in Fig. 9. With the integration of all enhanced modules, our system achieves impressive

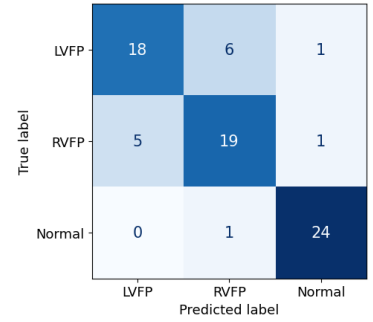


Fig. 10: Confusion matrix for the UVFP classification on the SYSU-A test dataset.

performance, with all metrics surpassing the 82% threshold, affirming its proficiency in distinguishing left from right VFP. An ablation study further corroborates these findings. The table illustrates that the adoption of quadratic fitting techniques significantly hones classification accuracy, as reflected by the enhancement in performance metrics. The addition of diffusion-based refinement also contributes to superior classification outcomes, excelling beyond the baseline model across all performance metrics. Moreover, the confusion matrix (Fig. 9) clearly shows the benefits of integrating the two enhanced modules. In comparison to the baseline model, which demonstrates a high rate of misclassification from left to right VFP and a lower rate in the opposite direction, the system predominately predicts right VFP over left VFP. However, this bias is substantially mitigated by the integration of both quadratic fitting and diffusion-based refinement techniques, showing a better classification result.

To further illustrate the efficacy of our system, we replace the oracle VFP labels with predictions from the initial multimodal VFP model (outlined in Section V-B and results shown in Section VI-E). Subsequently, in the second phase, we differentiate the system VFP cases into left or right VFP by analyzing the variance between LVFDyn and RVFDyn. The confusion matrices depicted in Fig. 10 present the comprehensive three-category classification outcomes. As depicted in Fig. 10, the majority of the samples were correctly identified, with the largest numbers in the confusion matrices forming their diagonals, showing an accuracy of 81.3%.

G. Auxiliary Visual Analysis for UVFP

In this subsection, the potential of the novel feature is demonstrated through expert visual analysis. Figure 11 showcases the GAW and VFDyn plots for a patient diagnosed with right VFP from the SYSU-A dataset. The MLVAS system extracts several video highlights, yielding multiple analytical outcomes. The left three figures present the time-normalized GAW, illustrating the global vibratory behavior of the vocal folds during phonation. However, these plots are not capable of differentiating between the movements of the individual vocal folds, thus clinicians are unable to ascertain the paralyzed vocal fold based solely on the GAW. In contrast, the VFDyn analysis, depicted in the figures listed vertically on the right, offers a disambiguated view of each vocal fold's motion. This granular perspective significantly augments the utility of the

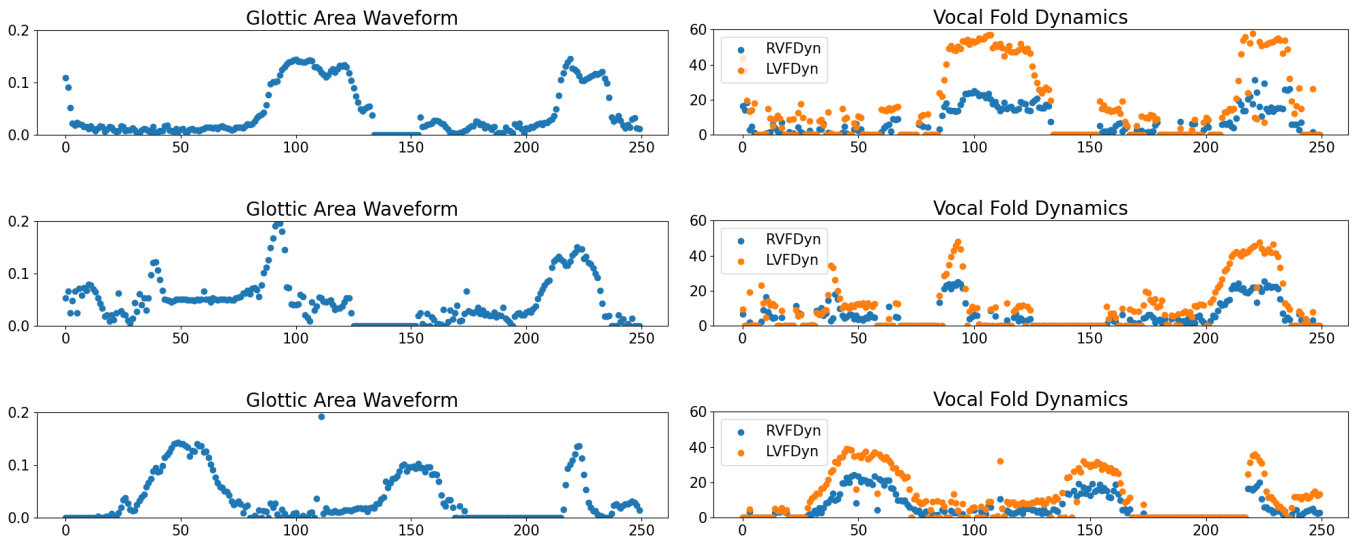


Fig. 11: The example charts of the extracted GAW and VFDyn from MLVAS for patient#7530 in the SYSU-A dataset, diagnosed as right VFP. There are three video highlights automatically extracted by the MLVAS (listed vertically). Thus, three different pairs of charts are extracted, with each pair contains a GAW chart and VFDyn chart listed horizontally.

metrics provided by the MLVAS for clinical assessment of UVFP. In this specific example, the VFDyn plots display a markedly greater level of oscillation for the LVFDyn in comparison to the RVFDyn, which is consistent with the patient’s right VFP diagnosis, thus validating the clinical utility of the MLVAS-derived metrics.

VII. CONCLUSION

In this work, we present the Multimodal Laryngoscopic Video Analyzing System (MLVAS), a novel framework that integrates both audio and image processing for enhanced diagnosis of laryngeal disorders. The system employs an audio-based KWS model to capture the full phonation cycle and a vocal fold image detection module to verify vocal folds’ existence. Through HSV color space analysis, MLVAS can extract stroboscopic sequences. As a result, MLVAS enables the automatic generation of video highlights from raw laryngoscopic footage, thus providing a practical diagnostic tool that removes the need for manual pre-editing. Objective metrics for clinical assessment are obtained by a two-stage segmentation process with an initial U-Net model-based segmentation followed by a diffusion model refinement, significantly reducing false positives caused by the initial U-Net segmentation. MLVAS continues with an unsupervised feature extraction approach, applying quadratic fitting to determine the glottal midline and then calculating the angle deviations for left and right vocal folds for all time frames — termed LVFDyn and RVFDyn. Uniting audio and image features, the system adopts a multimodal method for predicting UVFP, showing its effectiveness on a challenging clinical dataset. Furthermore, MLVAS enhances clinical interpretation with visualizations such as GAW and VFDyn, thus equipping clinicians with precise and efficient tools for UVFP diagnosis.

VIII. ACKNOWLEDGMENT

This research is funded by the DKU foundation project “Interdisciplinary Signal Processing Technologies”.

REFERENCES

- [1] A. Wilson, E. E. Kimball, L. Sayce, H. Luo, S. M. Khosla, and B. Rousseau, “Medialization laryngoplasty: A review for speech-language pathologists.” *Journal of speech, language, and hearing research : JSLHR*, pp. 1–10, 2021. [Online]. Available: <https://api.semanticscholar.org/CorpusID:231756615>
- [2] T. E. Havas, D. S. G. Lowinger, and J. Priestley, “Unilateral vocal fold paralysis: causes, options and outcomes.” *The Australian and New Zealand journal of surgery*, vol. 69 7, pp. 509–13, 1999. [Online]. Available: <https://api.semanticscholar.org/CorpusID:739826>
- [3] L. H. S. Rosenthal, M. S. Benninger, and R. H. Deeb, “Vocal fold immobility: A longitudinal analysis of etiology over 20 years.” *The Laryngoscope*, vol. 117, 2007. [Online]. Available: <https://api.semanticscholar.org/CorpusID:25645304>
- [4] R. R. Casiano, V. Zaveri, and D. S. Lundy, “Efficacy of videostroboscopy in the diagnosis of voice disorders,” *Otolaryngology–Head and Neck Surgery*, vol. 107, no. 1, pp. 95–100, 1992.
- [5] C. Tao, Y. Zhang, and J. J. Jiang, “Extracting physiologically relevant parameters of vocal folds from high-speed video image series,” *IEEE Transactions on Biomedical Engineering*, vol. 54, no. 5, pp. 794–801, 2007.
- [6] J. Donhauser, B. Tur, and M. Döllinger, “Neural network-based estimation of biomechanical vocal fold parameters,” *Frontiers in Physiology*, vol. 15, p. 1282574, 2024.
- [7] M. Pedersen, C. F. Larsen, B. Madsen, and M. Eeg, “Localization and quantification of glottal gaps on deep learning segmentation of vocal folds,” *Scientific Reports*, vol. 13, no. 1, p. 878, 2023.
- [8] A. S. Hamad, Y. Y. Wang, T. E. Lever, and F. Bunyak, “Ensemble of deep cascades for detection of laryngeal adductor reflex events in endoscopy videos,” in *Proceeding of the IEEE International Conference on Image Processing*. IEEE, 2020, pp. 300–304.
- [9] A. Hamad, M. Haney, T. E. Lever, and F. Bunyak, “Automated segmentation of the vocal folds in laryngeal endoscopy videos using deep convolutional regression networks,” in *Proceedings of the IEEE/CVF Conference on Computer Vision and Pattern Recognition Workshops*, 2019, pp. 0–0.

- [10] Y. Yan, D. Bless, and X. Chen, "Biomedical image analysis in high-speed laryngeal imaging of voice production," in *Proceeding of the 27th Annual International Conference on IEEE Engineering in Medicine and Biology*. IEEE, 2006, pp. 7684–7687.
- [11] J. Lin, E. S. Walsted, V. Backer, J. H. Hull, and D. S. Elson, "Quantification and analysis of laryngeal closure from endoscopic videos," *IEEE Transactions on Biomedical Engineering*, vol. 66, no. 4, pp. 1127–1136, 2018.
- [12] E. K. DeVore, N. Adamian, N. Jowett, T. Wang, P. Song, R. Franco, and M. R. Naunheim, "Predictive outcomes of deep learning measurement of the anterior glottic angle in bilateral vocal fold immobility," *The Laryngoscope*, vol. 133, no. 9, pp. 2285–2291, 2023.
- [13] R. Schwarz, U. Hoppe, M. Schuster, T. Wurzbacher, U. Eysholdt, and J. Lohscheller, "Classification of unilateral vocal fold paralysis by endoscopic digital high-speed recordings and inversion of a biomechanical model," *IEEE Transactions on Biomedical Engineering*, vol. 53, no. 6, pp. 1099–1108, 2006.
- [14] O. Gloger, B. Lehnert, A. Schrade, and H. Völzke, "Fully automated glottis segmentation in endoscopic videos using local color and shape features of glottal regions," *IEEE Transactions on Biomedical Engineering*, vol. 62, no. 3, pp. 795–806, 2014.
- [15] N. Adamian, M. R. Naunheim, and N. Jowett, "An open-source computer vision tool for automated vocal fold tracking from videoendoscopy," *The Laryngoscope*, vol. 131, no. 1, pp. E219–E225, 2021.
- [16] T. V. Wang, N. Adamian, P. C. Song, R. A. Franco, M. N. Huston, N. Jowett, and M. R. Naunheim, "Application of a computer vision tool for automated glottic tracking to vocal fold paralysis patients," *Otolaryngology–Head and Neck Surgery*, vol. 165, no. 4, pp. 556–562, 2021.
- [17] W. Pennington-FitzGerald, A. Joshi, E. Honzel, I. Hernandez-Morato, M. J. Pitman, and Y. Moayedi, "Development and application of automated vocal fold tracking software in a rat surgical model," *The Laryngoscope*, vol. 134, no. 1, pp. 340–346, 2024.
- [18] R. Islam, M. Tarique, and E. Abdel-Raheem, "A survey on signal processing based pathological voice detection techniques," *IEEE Access*, vol. 8, pp. 66749–66776, 2020.
- [19] J. D. Arias-Londono, J. I. Godino-Llorente, N. Sáenz-Lechón, V. Osma-Ruiz, and G. Castellanos-Domínguez, "Automatic detection of pathological voices using complexity measures, noise parameters, and mel-cepstral coefficients," *IEEE Transactions on Biomedical Engineering*, vol. 58, no. 2, pp. 370–379, 2010.
- [20] J. I. Godino-Llorente, P. G. Vilda, and M. Blanco-Velasco, "Dimensionality reduction of a pathological voice quality assessment system based on gaussian mixture models and short-term cepstral parameters," *IEEE Transactions on Biomedical Engineering*, vol. 53, no. 10, pp. 1943–1953, 2006.
- [21] M. E. Powell, M. Rodriguez Cancio, D. Young, W. Nock, B. Abdelmesih, A. Zeller, I. Perez Morales, P. Zhang, C. G. Garrett, D. Schmidt *et al.*, "Decoding phonation with artificial intelligence (dep ai): Proof of concept," *Laryngoscope Investigative Otolaryngology*, vol. 4, no. 3, pp. 328–334, 2019.
- [22] H.-C. Hu, S.-Y. Chang, C.-H. Wang, K.-J. Li, H.-Y. Cho, Y.-T. Chen, C.-J. Lu, T.-P. Tsai, and O. K.-S. Lee, "Deep learning application for vocal fold disease prediction through voice recognition: preliminary development study," *Journal of Medical Internet Research*, vol. 23, no. 6, p. e25247, 2021.
- [23] H. Wu, J. Soraghan, A. Lowit, and G. Di Caterina, "Convolutional neural networks for pathological voice detection," in *Proceeding of the 40th Annual International Conference of the IEEE Engineering in Medicine and Biology Society*. IEEE, 2018, pp. 1–4.
- [24] Z. Chuang, X. Yu, J. Chen, Y. Hsu, Z. Xu, C. Wang, F. Lin, and S. Fang, "Dnn-based approach to detect and classify pathological voice," in *Proceeding of the IEEE BigData*. IEEE, 2018, pp. 5238–5241.
- [25] D. M. Low, V. Rao, G. Randolph, P. C. Song, and S. S. Ghosh, "Identifying bias in models that detect vocal fold paralysis from audio recordings using explainable machine learning and clinician ratings," *medRxiv*, 2020.
- [26] E. C. Compton, T. Cruz, M. Andreassen, S. Beveridge, D. Bosch, D. R. Randall, and D. Livingstone, "Developing an artificial intelligence tool to predict vocal cord pathology in primary care settings," *The Laryngoscope*, vol. 133, no. 8, pp. 1952–1960, 2023.
- [27] J. Long, E. Shelhamer, and T. Darrell, "Fully convolutional networks for semantic segmentation," in *Proceedings of the IEEE Conference on Computer Vision and Pattern Recognition*, 2015, pp. 3431–3440.
- [28] O. Ronneberger, P. Fischer, and T. Brox, "U-net: Convolutional networks for biomedical image segmentation," in *Proceeding of the 18th International Conference on Medical Image Computing and Computer-Assisted Intervention part III 18*. Springer, 2015, pp. 234–241.
- [29] F. J. P. Montalbo, "S3ar u-net: A separable squeezed similarity attention-gated residual u-net for glottis segmentation," *Biomedical Signal Processing and Control*, vol. 92, p. 106047, 2024.
- [30] O. Oktay, J. Schlemper, L. L. Folgoc, M. Lee, M. Heinrich, K. Misawa, K. Mori, S. McDonagh, N. Y. Hammerla, B. Kainz, B. Glocker, and D. Rueckert, "Attention u-net: Learning where to look for the pancreas," in *Proceeding of Medical Imaging with Deep Learning*, 2018. [Online]. Available: <https://openreview.net/forum?id=Skft7cjm>
- [31] A. Hackman, C.-H. Chen, A. W.-G. Chen, and M.-K. Chen, "Automatic segmentation of membranous glottal gap area with u-net-based architecture," *The Laryngoscope*, 2024.
- [32] M. Döllinger, T. Schraut, L. A. Henrich, D. Chhetri, M. Echternach, A. M. Johnson, M. Kunduk, Y. Maryn, R. R. Patel, R. Samlan *et al.*, "Re-training of convolutional neural networks for glottis segmentation in endoscopic high-speed videos," *Applied Sciences*, vol. 12, no. 19, p. 9791, 2022.
- [33] X. Wei, Z. Deng, X. Zheng, B. He, and Y. Hu, "Weakly supervised glottis segmentation on endoscopic images with point supervision," *Biomedical Signal Processing and Control*, vol. 92, p. 106113, 2024.
- [34] H. Huang, L. Lin, R. Tong, H. Hu, Q. Zhang, Y. Iwamoto, X. Han, Y.-W. Chen, and J. Wu, "Unet 3+: A full-scale connected unet for medical image segmentation," in *Proceeding of the IEEE International Conference on Acoustics, Speech and Signal Processing*. IEEE, 2020, pp. 1055–1059.
- [35] A. O. Vuola, S. U. Akram, and J. Kannala, "Mask-rcnn and u-net ensembled for nuclei segmentation," in *Proceeding of the IEEE 16th International Symposium on Biomedical Imaging*. IEEE, 2019, pp. 208–212.
- [36] P. F. Jaeger, S. A. Kohl, S. Bickelhaupt, F. Isensee, T. A. Kuder, H.-P. Schlemmer, and K. H. Maier-Hein, "Retina u-net: Embarrassingly simple exploitation of segmentation supervision for medical object detection," in *Machine Learning for Health Workshop*. PMLR, 2020, pp. 171–183.
- [37] K. Inagi, A. A. Khidr, C. N. Ford, D. M. Bless, and D. M. Heisey, "Correlation between vocal functions and glottal measurements in patients with unilateral vocal fold paralysis," *The Laryngoscope*, vol. 107, no. 6, pp. 782–791, 1997.
- [38] D. DeChance, E. Frank, S. Dehom, W. Watson, E. Simmons, P. D. Krishna, and B. Crawley, "Clinical and anatomical variation during assessment of maximum glottic angle," *The Laryngoscope*, vol. 134, no. 6, pp. 2793–2798, 2024.
- [39] E. Kruse, M. Döllinger, A. Schützenberger, and A. M. Kist, "Glottis-netv2: temporal glottal midline detection using deep convolutional neural networks," *IEEE Journal of Translational Engineering in Health and Medicine*, vol. 11, pp. 137–144, 2023.
- [40] A. M. Kist, J. Zilker, P. Gómez, A. Schützenberger, and M. Döllinger, "Rethinking glottal midline detection," *Scientific reports*, vol. 10, no. 1, p. 20723, 2020.
- [41] K. He, X. Zhang, S. Ren, and J. Sun, "Deep residual learning for image recognition," in *Proceedings of the IEEE Conference on Computer Vision and Pattern Recognition*, 2016, pp. 770–778.
- [42] G. Jocher, "Ultralytics yolov5," 2020. [Online]. Available: <https://github.com/ultralytics/yolov5>
- [43] P. Gómez, A. M. Kist, P. Schlegel, D. A. Berry, D. K. Chhetri, S. Dürr, M. Echternach, A. M. Johnson, S. Kniesburges, M. Kunduk *et al.*, "Bagls, a multihospital benchmark for automatic glottis segmentation," *Scientific Data*, vol. 7, no. 1, p. 186, 2020.
- [44] J. Ho, A. Jain, and P. Abbeel, "Denosing diffusion probabilistic models," *Advances in Neural Information Processing Systems*, vol. 33, pp. 6840–6851, 2020.
- [45] L. Yang, Z. Zhang, Y. Song, S. Hong, R. Xu, Y. Zhao, W. Zhang, B. Cui, and M.-H. Yang, "Diffusion models: A comprehensive survey of methods and applications," *ACM Computing Surveys*, vol. 56, no. 4, pp. 1–39, 2023.
- [46] J. Wu, R. Fu, H. Fang, Y. Zhang, Y. Yang, H. Xiong, H. Liu, and Y. Xu, "Medsegdiff: Medical image segmentation with diffusion probabilistic model," in *Proceeding of Medical Imaging with Deep Learning*. PMLR, 2024, pp. 1623–1639.
- [47] M. Tan and Q. Le, "Efficientnet: Rethinking model scaling for convolutional neural networks," in *Proceeding of International Conference on Machine Learning*. PMLR, 2019, pp. 6105–6114.
- [48] X. Shi, Z. Chen, H. Wang, D.-Y. Yeung, W.-K. Wong, and W.-c. Woo, "Convolutional lstm network: A machine learning approach for precipitation nowcasting," *Advances in Neural Information Processing Systems*, vol. 28, 2015.